Check for updates

Electrocatalytic upcycling of nitrate and hydrogen sulfide via a nitrogen-doped carbon nanotubes encapsulated iron carbide electrode

Wanqiang Yu [a], Jiayuan Yu [a,*], Yujie Wang [a], Xiao Li [a], Yijie Wang [a], Haifeng Yuan [a], Xiaoli Zhang [b], Hong Liu [a,c], Weijia Zhou [a,*]

[a] *Collaborative Innovation Center of Technology and Equipment for Biological Diagnosis and Therapy in Universities of Shandong, Institute for Advanced Interdisciplinary Research (iAIR), University of Jinan, Jinan 250022, PR China*
[b] *School of Materials Science and Engineering, Zhengzhou University, Zhengzhou 450001, PR China*
[c] *State Key Laboratory of Crystal Materials, Shandong University, Jinan 250100, PR China*

ARTICLE INFO

ABSTRACT

To achieve the efficient electrocatalytic upgrading of nitrate (NO_3^-) and hydrogen sulfide (H_2S) to value-added ammonia (NH_3) and sulfur (S) from wastewater, herein, we report a remarkable nitrogen-doped carbon nanotubes encapsulated iron carbide array electrode ($Fe_3C@N$-CNTs/IF) as both cathode and anode for the efficient electrocatalytic reduction of NO_3^- to NH_3 and oxidation of H_2S to S, respectively. Both experimental and theoretical calculation confirm the high activity of $Fe_3C@N$-CNTs/IF. A maximal NH_3 faradaic efficiency of ~97.9% with the yield rate of 0.922 mg h^{-1} cm^{-2} at − 1.1 V vs. SCE and the S yield rate of 33.76 mg h^{-1} cm^{-2} at the current density of 100 mA cm^{-2} can be achieved. In addition, a flow cell is employed with a multifunctional $Fe_3C@N$-CNTs/IF electrode with channels made by laser to maintains excellent stability for continuous upcycling NO_3^- and H_2S to produce NH_3 and S, which demonstrates its massive potential for practical application.

1. Introduction

As one of the most momentous bulk chemicals discovered on earth, ammonia (NH_3) is not only applied as an essential ingredient for the production of fertilizer, synthon, dyes, etc., but also regarded as a promising alternative to fossil fuels for being high in hydrogen and carbon-free [1–5]. At present, NH_3 is mass produced through the highly-developed Haber-Bosch process, but this process is energy intensive and involves a harsh reaction environment requiring elevated temperature and high pressure. [6–11]. Due to the massive demand in market and the large scale of energy consumption, the energy use of modern industrial NH_3 production exceeds 1% of the global energy supply, with about 1% of carbon dioxide produced and discharged [12–14]. Therefore, it is imperative but still challenging to develop the technology that enables environmental-friendly NH_3 synthesis.

Powered by various renewable energy such as solar, wind and tidal energy, etc., the electrochemical NH_3 synthesis route is one of the most fascinating alternatives to Haber-Bosch process. Recently, there have been plenty of efforts made on the transformation of electrocatalytic nitrogen (N_2) into NH_3, where the N_2 obtained from the atmosphere is applied as one of the major nitrogen sources [15–20]. Despite a significant progress made in recent years for the research of nitrogen reduction reaction (NRR) catalysts with high activity and selectivity, the yield rate of NH_3 remains very low (mostly < 200 μg h^{-1} mg$_{cat}$$^{-1}$) due to the low solubility of N_2 in electrolyte [1,21–24]. Obtained from various sources, including industrial wastewater, liquid nuclear waste, livestock manure and chemical fertilizer, nitrate ion (NO_3^-) has a wide concentration range of up to about 2 M, and it is a widely distributed water pollutants in the world [25]. For example, it is a common practice in machinery, chemical industry, electroplating, photovoltaic and other industries to use nitric acid or nitrate as raw materials and auxiliary agents, which causes the high levels of nitrate concentration in wastewater [26]. Besides, the nitrogen-containing organic substances are usually used in large amounts in the food processing, leather, paper-making, chemical fertilizer and other industries, which is an indirect cause for the nitrate pollution occurring after decomposition in wastewater [27]. At present, the mainstream methods of NO_3^- treatment include biodegradation, chemical reduction, adsorption enrichment and so on, with NO_3^- selectively reduced to N_2 with low added-value [28–31]. Recently, it has been shown in more and more studies that

the efficient synthesis of NH_3 can be achieved through nitrate reduction reaction (NIRR), for its recycling [32,33]. Over the years, there have been various metals and their alloys explored for the efficient conversion of NO_3^- into NH_3. Among them, iron-based catalysts have attracted extensive attention for NIRR due to their high catalytic activity [27, 34–36]. However, the inevitable oxidation and corrosion of iron-based catalysts make its poor stability in aqueous media one of the constraints on its development. In recent years, some studies have been conducted on such a strategy, that is, through the construction of a series of core-shell structured catalysts, such as 3d transition metals or their compounds encapsulated in carbon nanotubes or graphitic carbon layers, the inner active catalyst can be effectively protected against corrosion in various harsh environment [37–39]. As suggested by Qian et al., FeNi/g-mesoc/NF can be used to efficiently transform NO_3^- and maintain stability for a long time [38]. Yang et al. used carbon layer to wrap the iron nanoparticles self-assembled into micron spheres for use as an excellent NO_3^- reduction catalyst [25]. Despite some research and progress in relation to electrochemical NO_3^- reduction, it remains a challenge to achieve efficient and selective electrochemical reduction in practice.

Although the preparation of NH_3 by electrochemical NO_3^- reduction is a promising NO_3^- treatment technology, especially with the development of clean electric energy technology, a large amount of additional power is consumed due to the slow oxygen evolution reaction (OER) at anode, and the product is low-value oxygen [40–42]. Therefore, a lot of previous studies focused on the alternative reaction of anode OER for the purpose of reducing power consumption and obtaining high value-added products [43,44]. The hydrogen sulfide (H_2S) oxidation reaction (SOR) is regarded as a promising alternative reaction because it is easier to achieve than OER in thermodynamics. In addition, H_2S is generally accepted as a hazardous substance. The primary causes of H_2S pollution are natural gas purification, sulfide dyes, papermaking and other production processes [37]. At the same time, there are also some indirect contributors to it, including the corruption of organic biomass and the transformation of sulfate in wastewater under the action of microorganisms. The electrochemical oxidation of H_2S at the anode side can lead to the degradation of pollutants for the preparation of high value-added S while reducing energy consumption [45]. In fact, nitrate and H_2S coexist in the wastewater resulting from various industrial production processes, such as papermaking [46]. Therefore, SOR and NIRR can be combined to achieve the simultaneous recycling and utilization of resources at low energy costs.

Herein, we reported a laser-assisted synthetic Fe_3C nanoparticle encapsulated into nitrogen-doped carbon nanotubes array on iron foil ($Fe_3C@N-CNTs/IF$) as a binder-free electrode and evaluated its electrocatalytic performance of NIRR and SOR. In the course of preparing $Fe_3C@N-CNTs/IF$, the ultraviolet (UV) laser was used to produce catalyst. Due to its suitability for cold work, the possibility of strong thermal effect can be eliminated, which allows rapid and large-area preparation. $Fe_3C@N-CNTs/IF$ reached a maximum NH_3 faradaic efficiency (FE) of ~97.9% at − 1.1 V vs. SCE and NH_3 yield rate of ~0.922 mg h^{-1} cm^{-2}. According to density functional theory (DFT) calculations, NO_3^- adsorption and activation are the potential limiting steps. Importantly, a proof-of-concept electrochemical flow reactor was designed and assembled to involve porous $Fe_3C@N-CNTs/IF$ in electrochemical NO_3^- reduction. In order to reduce the electrolytic voltage of double electrode system, the SOR performance of $Fe_3C@N-CNTs/IF$ was tested. By using $Fe_3C@N-CNTs/IF$ as a bifunctional catalyst and coupling SOR on anode and NIRR on cathode, NO_3^- and H_2S were converted into NH_3 and S with high added-value products at the voltage of 1.1 V.

2. Experimental section

2.1. Chemicals

Hydrochloric acid (HCl), Sodium sulfate (Na_2SO_4) were purchased

from Sinopharm Chemical Reagent Co., Ltd. Sodium nitrite ($NaNO_3$), Sulfamic acid (H_3NO_3S), Sodium hypochlorite (NaClO), Sodium nitro-ferricyanide dihydrate ($C_5FeN_6Na_2O\cdot 2H_2O$), Sodium hydroxide (NaOH), Salicylic acid ($C_7H_6O_3$), Potassium sodium tartrate tetrahydrate ($C_4H_4O_6KNa\cdot 4H_2O$), Phosphoric acid (H_3PO_4), Sulfanilamide ($C_6H_8N_2O_2S$), N-(1-naphthyl) ethylenediamine dihydrochloride ($C_{12}H_{14}N_2\cdot 2HCl$), Sodium nitrite ($NaNO_2$), Ammonium chloride ($NH_4Cl$), Carbon nanotube bundled multi-walled, Sodium sulfide (Na_2S) were purchased from Shanghai Macklin Biochemical Co., Ltd. The Thermo Scientific Barnstead Smar2Pure Ultrapure Water System (18.2 MΩ cm) was used to produce deionized water. Iron foils were purchased from Dahe New Energy Co., Ltd. Unless otherwise stated, all reagents were used without further purification.

2.2. Synthesis of samples

2.2.1. Synthesis of Fe nanoparticles loaded on the Fe foil (Fe NPs/IF)

To begin with, pristine Fe foil was ultrasonically cleaned in absolute ethanol and deionized water respectively. The fabrication of Fe NPs/IF with a specific pattern was carried out using a nanosecond pulsed UV laser device (Pulse 355–3, Shanghai Fermi Laser Technology Co., Ltd.) with the wavelength of 355 nm, which was also equipped with a vacuum pump to keep the metal sheets in close-contact. The specific parameters and pattern design of the laser were controlled by a software (called EzCad2) installed on the computer. A linear scanning mode with the repetition rate of 20 kHz, scanning spacing of 0.001 mm, scanning speed of 200 mm s^{-1} and laser power of 0.75 W was set up for the patterning of laser. Before determining the final sample, laser power (0.15, 0.3, 0.45, 0.6, 0.75, 0.9 W) was optimized, the results were shown in Fig. S1, respectively.

2.2.2. Synthesis of Fe3C nanoparticles embedded N-doped carbon nanotubes on the Fe foil (Fe3C@N-CNTs/IF)

For the synthesis of $Fe_3C@N-CNT/IF$, 120 mg dicyandiamide was placed at one end of the porcelain boat and the square shaped Fe NPs/IF with a side length of 1 cm was prepared using laser was placed at the other end. The porcelain boat was sealed with copper foil and then placed into the quartz tube. When argon was introduced into the quartz tube, ensure that the end of dicyandiamide is located at the upper gas outlet. place it in the center of the tubular furnace. The assembled quartz tube is heated by a tubular furnace. After 2 h of heating at 500 °C, the temperature was increased to 800 °C and maintained for 2 h, so that the final $Fe_3C@N-CNTs/IF$ was obtained. In addition, the $Fe_3C@N-CNTs/IF$ calcined at different temperatures (700, 800, 900, 1000 ℃) were labeled as $Fe_3C@N-CNTs/IF-700$, $Fe_3C@N-CNTs/IF-800$, $Fe_3C@N-CNTs/IF-900$ and $Fe_3C@N-CNTs/IF-1000$, respectively. Moreover, the $Fe_3C@N-CNTs/IF$ calcined with Fe NPs/IF at different laser power (0.15, 0.3, 0.45, 0.6, 0.75, 0.9 W) were also obtained, the results of which are shown in Fig. S1 and Fig. S2.

2.2.3. Synthesis of porous Fe3C nanoparticles embedded N-doped carbon nanotubes on the Fe foil (porous Fe3C@N-CNTs/IF)

Fe NPs/IF was prepared using the above-mentioned method. For the electrolyte to pass through, the prepared Fe NPs/IF was punched with a 1.35 W laser power, named porous Fe NPs/IF. The radius of the hole is controlled at 50 μm, and the hole spacing is set to 50 μm. Then, porous $Fe_3C@N-CNTs/IF$ was prepared by the same method with dicyandiamide and Fe NPs/IF as precursors.

2.2.4. Synthesis of the comparison materials

The synthesis steps of the comparison materials ($Fe_3C@CNTs/IF$ and N-CNTs/IF) were presented in the Text S1 in Supporting information.

2.3. Characterization

The crystal structure of the prepared electrocatalysts were

determined by Smartlabse (RIGAKU) X-ray diffractometer (XRD) with Cu Kα radiation (λ = 0.15406 nm). The microstructure and morphology were clarified by Regulus 8100 (HITACHI) Field Emission Scanning Electron Microscope (FESEM) and JEM-2100 F (JEOL) transmission electron microscope (TEM) at an acceleration voltage of 200 kV. The elemental composition and chemical environment of the materials were characterized by Axis Supra (Kratos) X-ray photoelectron spectroscopic (XPS). Raman spectra were collected using a LabRAM HR Evolution spectrometer (Horiba). A UV–vis spectrophotometer (EVOLUTION 201, Thermo Scientific Corporation) measurements in the range of 200–1000 nm.

2.4. Electrochemical measurements

2.4.1. Electrochemical measurements of nitrate reduction reaction (NIRR)

The electrochemical measurements were carried out using a CHI 760E electrochemical workstation (Chenhua, Shanghai) in a H-type electrolytic cell separated by a membrane. The $Fe_3C@N$-CNTs/IF, saturated calomel electrode (SCE) and platinum foil was used as the working electrode, reference electrode and counter electrode, respectively. The surface area of the working electrode was controlled with 1 cm^2. 0.5 M Na_2SO_4 solution (50 mL) was evenly distributed to the cathode and anode compartment. $NaNO_3$ was added into the cathode compartment for NO_3^- reduction (containing 200 ppm nitrate-N). Before nitrate electroreduction test, Linear sweep voltammetry (LSV) curves are performed until that the polarization curves achieve steady-state ones at a rate of 10 mV s^{-1} from − 0.6 to − 1.4 V. Then, the potentiostatic test was carried out at different potentials for 2 h with a stirring rate of 300 rpm.

2.4.2. Electrochemical measurements of sulfide oxidation reaction (SOR)

The electrocatalytic properties toward SOR were studied in Ar-saturated 1.0 M NaOH with or without 1.0 M Na_2S by using a two-chambers three-electrode device, in which the $Fe_3C@N$-CNTs/IF was applied as working electrode, and Hg/HgO (1.0 M KOH) and platinum foil were used as reference electrode and as counter electrode, respectively. Linear sweep voltammetry (LSV) curves were performed until that the polarization curves achieve steady-state ones at a rate of 10 mV s^{-1} from 0 to 2.0 V. Then, the potentiostatic test was carried out at a current density of 100 mA cm^{-2} for 36 h with a stirring rate of 300 rpm.

2.5. Determination of ion concentration

The ultraviolet-visible (UV-Vis) spectrophotometer was used to detect the ion (nitrate-N, nitrite-N, ammonia-N and short-chain polysulfides (S_2^{2-}-S_4^{2-})) concentration of pre-test and post-test electrolytes

after diluting to appropriate concentration to match the range of calibration curves. The specific detection methods were presented in the Text S2 in Supporting information.

2.6. Computational method

All the density functional theory (DFT) calculations in this work were performed by Vienna Ab-initio Simulation Package (VASP), using the Projected Augmented Wave (PAW) method. More details are presented in the Text S3 in Supporting information.

### 3. Results and discussion

3.1. Synthesis process of $Fe_3C@N$-CNTs/IF

The fabrication processes of iron carbide (Fe_3C, a typical Fe-based interstitial compound) nanoparticles embedded in nitrogen-doped carbon nanotubes (N-CNTs) array on iron foil ($Fe_3C@N$-CNTs/IF) is schematic illustrated in Fig. 1. After the polishing and cleaning of IF, the UV laser beam (3 W, 355 nm) was irradiated on the surface of iron foil (IF) to obtain an active Fe nanoparticles layer (referred to Fe NPs/IF). Notably, the laser treatment played a crucial role in the successful preparation of $Fe_3C@N$-CNTs/IF, as detailed in Fig. 2. As for the operational parameters effect of the morphology and properties, it was discussed in depth, as detailed in Fig. S1, S2 and Text S4 as Supporting information. Then, the finial sample was obtained by following a simple heat treatment process. To be specific, both Fe NPs/IF and dicyandiamide were placed in a porcelain boat with cover together and then calcined at 800 ℃ for 2 h in a furnace under argon atmosphere flow. Finally, the multifunctional $Fe_3C@N$-CNTs/IF was obtained and employed as cathode for electro-reduction of NO_3^- to NH_3 and as anode for electrocatalytic oxidation H_2S to S. The $Fe_3C@N$-CNTs/IF electrodes with holes as prepared by laser drilling were used to construct the proof-of-concept home-made flow cell, while achieving the recovery of dual pollutants (NO_3^- and H_2S) to high value-added products (NH_3 and S) during continuous reaction.

3.2. Microstructure characterization of $Fe_3C@N$-CNTs/IF

The morphology of relevant samples was firstly characterized by field emission scanning electron microscopy (FESEM). In order to highlight the critical role of laser pretreatment in the successful synthesis of $Fe_3C@N$-CNTs/IF, a patterned design electrode was adopted. The corresponding digital images of Fe NPs/IF are shown in Fig. 2a. The brown "NIRR" area represented the part processed by the UV laser. As shown in Fig. 2b, the untreated part of IF had a smooth surface. In
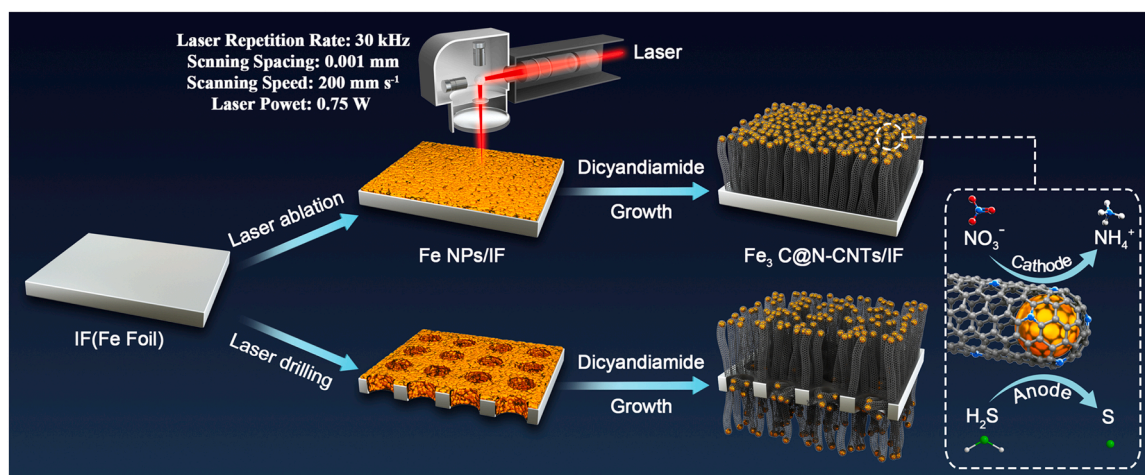
Fig. 1. The schematic diagram of synthetic procedure of $Fe_3C@N$-CNTs/IF electrode.
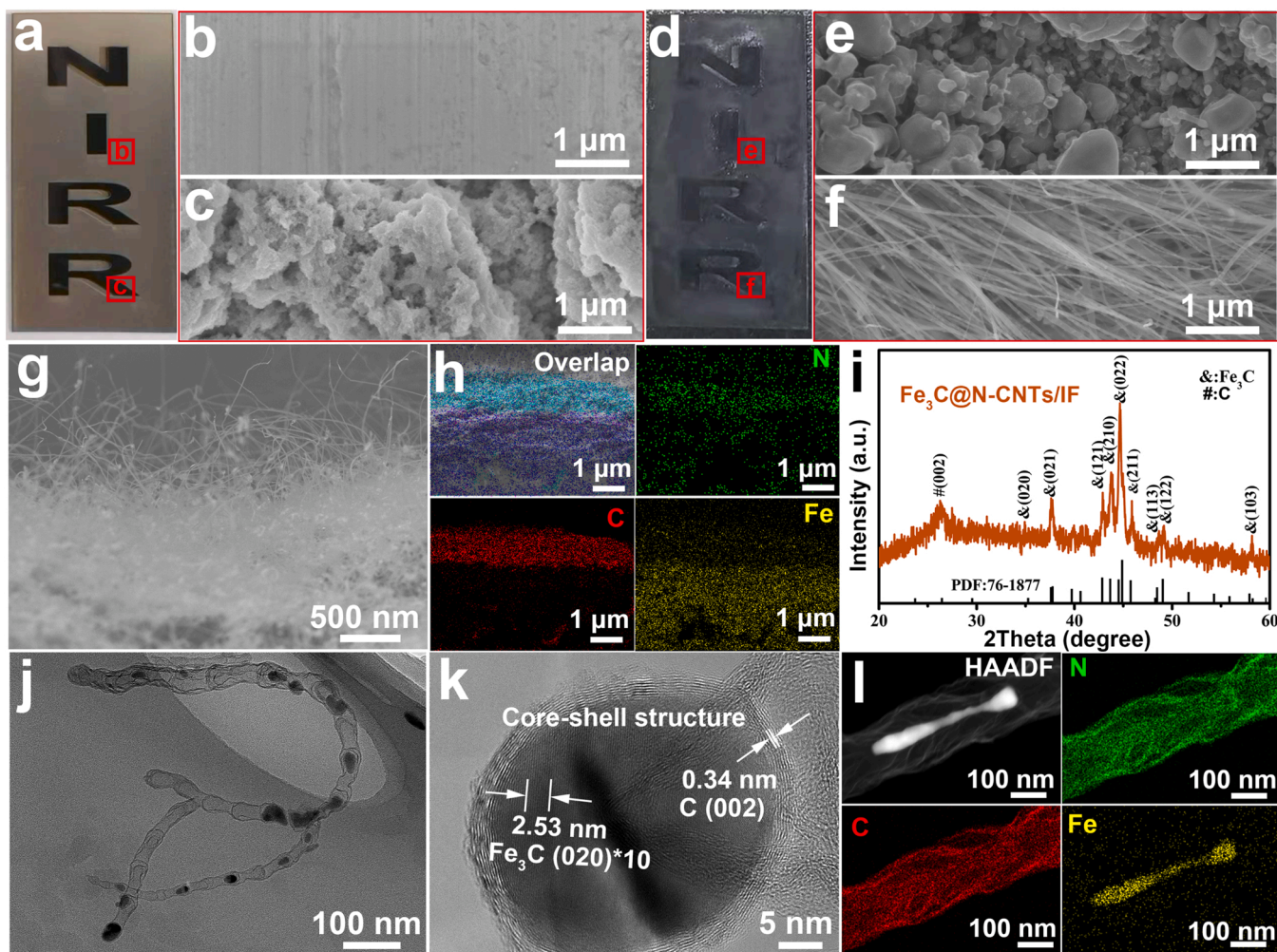
Fig. 2. Digital photograph and FESEM images of the selected area: (a-c) Fe NPs/IF and (d-f) Fe₃C@N-CNTs/IF. (g) Side view FESEM, (h) according FESEM-EDS element mapping images and (i) XRD pattern of Fe₃C@N-CNTs/IF. (j) TEM image, (k) HRTEM images and (l) TEM-EDS element mappings of N, C, and Fe for Fe₃C@N-CNTs.

contrast, the laser-treated section presented an uneven surface (Fig. 2c), where a large number of visible nanoparticles existed. Subsequently, these nanoparticles were confirmed as Fe NPs by X-ray diffraction (XRD) pattern (Fig. S3). After the carbonization of Fe NPs/IF with dicyandiamide, the overall color of the electrode turned black (Fig. 2d). However, there were no N-CNTs observed on the surface in the area not subjected to treatment (Fig. 2e). In contrast, from the FESEM image shown in Fig. 2f, it can be seen clearly that there were plenty of CNTs existing in the "NIRR" area, which indicated that the Fe NPs can be converted into Fe₃C@N-CNTs. According to the side view FESEM image and the EDS mapping of Fe₃C@N-CNTs/IF as presented in Fig. 2g, h, there was a tight interface existing between IF and Fe₃C@N-CNTs, and the thickness of Fe₃C@N-CNTs was measured to be 2–3 μm. These results indicated that the UV laser treatment of IF was essential for the successful generation of Fe₃C@N-CNT. With reference made to the previous studies, it can be known that the "tip-growth" mechanism applied to the formation of Fe₃C@N-CNTs/IF [47,48]. During heat treatment, the molten Fe NPs reacted with free carbon species to generate the Fe₃C nanoparticles of a small size. When the solubility of carbon species exceeded the saturation limit (6.69 wt%), the carbon species were dissolved out from Fe₃C nanoparticles. Finally, Fe₃C acted as the catalyst for the tip growth of N-CNTs and gave rise to Fe₃C@N-CNTs.

The crystal structure of Fe₃C@N-CNTs/IF was characterized by XRD (Fig. 2i). Except for the broad peak located at around 25° could be assigned to C (002), the other diffraction peaks, such as 26.3° (110),

37.8° (021), 42.9° (121), 43.8° (210) 44.6° (022), 45.9° (211), 48.6° (113), 49.2° (122) and 58.1° (130), corresponding clearly to the Fe₃C phases (JCPDS No. 76–1877, orthorhombic, a = 4.517 Å, b = 5.079 Å, c = 6.73 Å) [49,50]. To further demonstrate the microstructure of Fe₃C@N-CNTs, superficial substance was carefully scraped from the Fe₃C@N-CNTs/IF and then measured by transmission electron microscope (TEM). According to the TEM image in Fig. 2j, there were a large number of nanoparticles observed in CNTs, all of which were deduced as Fe₃C nanoparticles. And the particle size was mainly distributed in 20–30 nm (Fig. S4). As suggested by the high-resolution TEM (HRTEM) image presented in Fig. 2k, the inner nanoparticle was wrapped by ultrathin shell (about 1–2 nm), exhibiting a typical core-shell structure. The inner nanoparticle with the lattice fringes spacing of 0.253 nm was shown to be well matched with the (020) of Fe₃C, while the ultrathin shell with the lattice fringes spacing of 0.34 nm was found corresponding to the (002) lattice plane of graphite. As confirmed by the EDS elements mapping of the Fe₃C@N-CNTs, both nitrogen and carbon were uniformly distributed in the CNT. The successful doping of nitrogen into CNT is demonstrated in Fig. 2l. Differently, the Fe and C elements as derived from Fe₃C nanoparticle were encapsulated in N-CNT. Noticeably, this unique core-shell structure (Fe₃C@N-CNTs) possessed the following advantages. On the one hand, the inert ultrathin graphite layer could serve as a protective layer to prevent the inner Fe₃C nanoparticles from severe corrosion in the harsh electrolyte. On the other hand, the very thin carbon shell (1–2 nm) could facilitate the electrons originating

from the inner Fe_3C to pass through to the outer carbon layer, thus making the carbon layer show catalytic activity toward NIRR.

The Raman spectroscopy was measured to further explore the characteristics of carbon of the $Fe_3C@N$-CNTs/IF. As shown in Fig. S5, the peaks were detected at 1592 and 1351 cm^{-1}, corresponding to the G-band and D-band, respectively. By comparing the intensity of these two peaks, it can be discovered that the value of I_D/I_G is 1.06, indicating plenty of lattice defects due to the N-doping [43]. Furthermore, the 2D-band around at 2805 cm^{-1} was also detected, indicating a part of graphene in the carbon shell existed in the form of multilayers in the $Fe_3C@N$-CNTs/IF. The chemical environment of each element in $Fe_3C@N$-CNTs/IF was characterized by X-ray photoelectron spectroscopy (XPS). The presence of Fe, C, O and N in $Fe_3C@N$-CNTs/IF was confirmed in Fig. S6a. The Fe 2p XPS spectrum is displayed in Fig. S6b, which reveals that both Fe^{2+} and Fe^{3+} species were present in $Fe_3C@N$-CNTs/IF [47,51]. In Fig. S6c, the peaks located at 398.5, 399.1, and 401.0 eV suggested the presence of pyridinic N, pyrrolic N, and graphitic N, respectively. At the same time, it was determined that the doping amount of N in $Fe_3C@N$-CNTs/IF was 6.9%. Furthermore, sp^2-C (284.5 eV), sp^3-C (285.0 eV), C-N (286.15 eV), and O-C=O (288.1 eV) can be identified from the C 1 s spectra (Fig. S6d). All the above results indicated the successful synthesis of $Fe_3C@N$-CNTs/IF.

3.3. Evaluating the NIRR performance of $Fe_3C@N$-CNTs/IF

The NIRR performance of $Fe_3C@N$-CNTs/IF was tested using a typical three-electrode system in Na_2SO_4 electrolyte with a certain amount of NO_3^-. The concentrations of feed and electrolytic products were analyzed by UV spectrophotometry. (Fig. S7) [32]. As shown in Fig. 3a, the current density between the potential range from -0.9 to -1.3 V vs. SCE was increased in the present of NO_3^-, which was ascribed to the occur of NIRR [52,53]. According to the analysis of LSV, a series of potentiostatic tests were carried out under different voltages in order to further accurately evaluate the NIRR performance of $Fe_3C@N$-CNTs/IF with NH_3 yields and FEs, as in Fig. 3b, c and S8, S9. From -0.9 to -1.3 V, the electrochemical reduction rate of NO_3^- showed an increasing trend, while the FE of NH_3 increased first and then decreased. Additionally, the maximum FE of NH_3 (97.9%) and the NH_3 yield rate of ~0.922 mg h^{-1} cm^{-2} were achieved at -1.1 V (Fig. 3c). The reaction rate of NIRR is displayed in Fig. 3d and S10. When the potentiostatic test was carried out at -1.1 V for 8 h, the NO_3^- content in the electrolyte declined to 110.90 ppm. In the contrary, the amount of NH_3 increased to 80.18 ppm, implying the continuous progress of NIRR. The increase of NO_3^- concentration from 100 to 8000 ppm made no difference to NH_3 FEs, indicating the wide NO_3^- concentration applicability of $Fe_3C@N$-CNTs/IF for NIRR (Fig. 3e and S11).

In order to assess the NIRR stability of the $Fe_3C@N$-CNTs/IF, cyclic
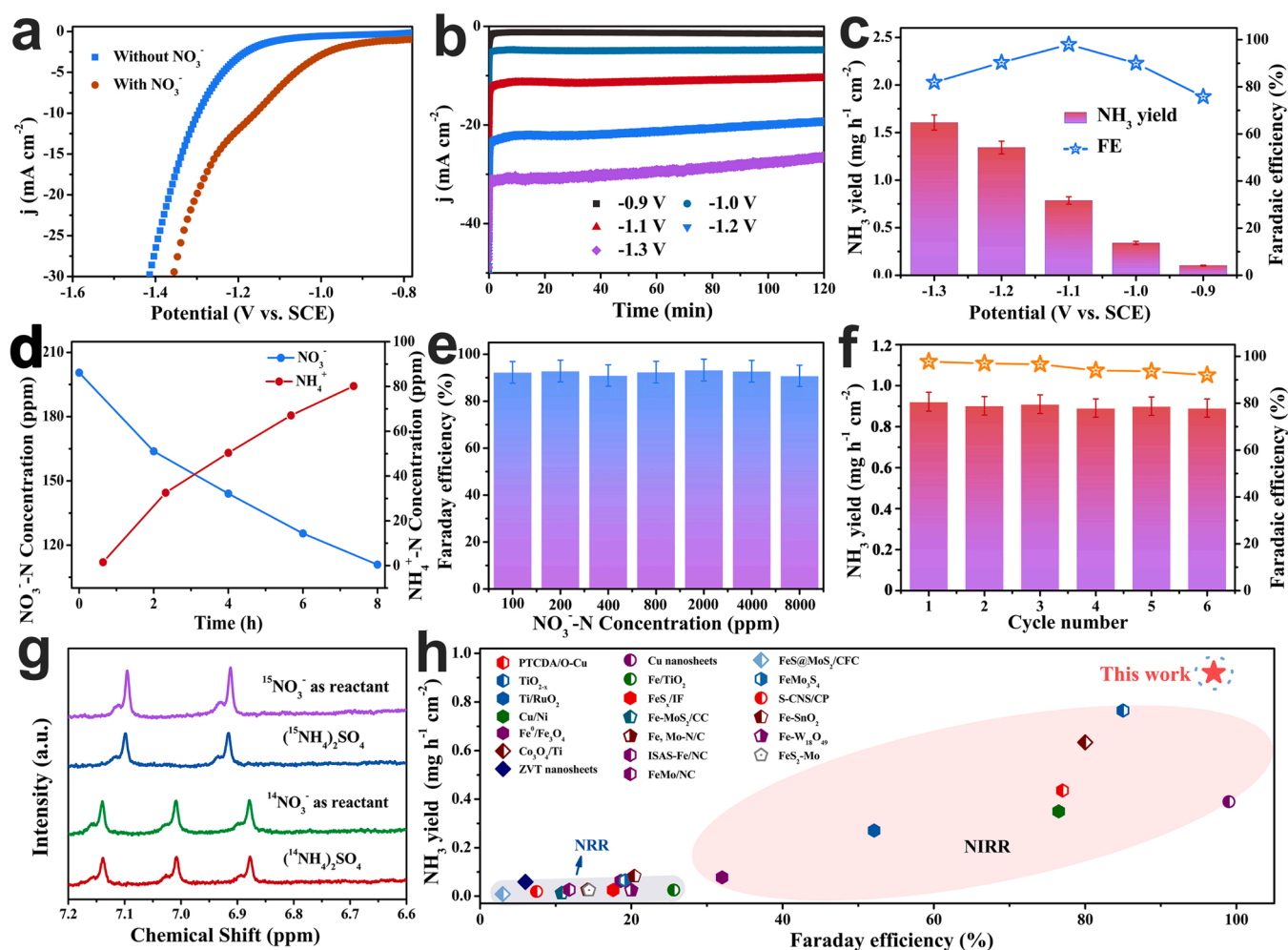
Fig. 3. NIRR performance of $Fe_3C@N$-CNTs/IF. (a) Polarization curves, (b) i-t curves against various work potentials, (c) NH_3 yield rates and FEs, (d) Time-dependent concentration change of NO_3^- and NH_3 yield. (e) Selectivity of NH_3 with different concentrations of NO_3^--N. (f) The consecutive recycle testing. (g) 1 H NMR spectra of the electrolyte after the NRR using $^{15}NO_3^-$ as the feedstock. (h) The comparison of the NH_3 yields and FEs of $Fe_3C@N$-CNTs/IF with the reported catalysts for the NRR and NIRR (Table S1 for detailed references).

test was conducted. There was no significant attenuation of the NH$_3$ yield or FEs after six cycles (Fig. 3f and S12), suggesting the high catalytic stability. Furthermore, the FESEM and XRD of Fe$_3$C@N-CNTs/IF showed no significant change after long-term tests (Fig. S13), which evidences its structural robustness. To demonstrate that the N in NH$_3$ comes from nitrate, isotopic labeling experiments were carried out using ^{15}NO$_3^-$ and ^{14}NO$_3^-$ as the reactant, respectively. The classic ^{15}NH$_3$ signal was detected by the ^{1}H nuclear magnetic resonance (NMR) spectrum with ^{15}NO$_3^-$ as feedstock (Fig. 3g), consistent with the ^{1}H NMR spectrum of (^{15}NH$_4$)$_2$SO$_4$ [54]. Meanwhile, with the use of ^{14}NO$_3^-$ as reactant in the electrolyte, the detection result of ^{1}H NMR was found consistent with that of (^{14}NH$_4$)$_2$SO$_4$. To sum up, these results suggested that the generation of NH$_3$ was attributed completely to NO$_3^-$ reduction. Furthermore, the performance of Fe$_3$C@N-CNTs/IF (~0.922 mg h^{-1} cm^{-2} @1.1 V vs. SCE) toward NIRR outperformed many recently reported nonprecious electrocatalysts as summarized in Fig. 3h and Table S1.

3.4. Active sites and reaction mechanisms of Fe$_3$C@N-CNTs/IF toward NIRR

To further understand the effects of structure and components of Fe$_3$C@N-CNTs on catalytic activity, the control samples of N-CNTs and Fe$_3$C@CNTs were synthesized, and the corresponding XRD patterns and FESEM images are shown in Figs. S14, S15, respectively [55]. The NIRR

performance of N-CNTs/IF and Fe$_3$C@CNTs/IF was recorded for comparion with Fe$_3$C@N-CNTs/IF. In Fig. 4a-c and Fig. S16, the inactive NIRR performance was evidenced by NO$_3^-$ conversion rate, NH$_3$ production rate and FEs of N-CNTs/IF (0.106 mg h^{-1} cm^{-2}, 0.0406 mg h^{-1} cm^{-2} and 36.79%) and Fe$_3$C@ CNTs/IF (0.197 mg h^{-1} cm^{-2}, 0.128 mg h^{-1} cm^{-2} and 54.55%). By contrast, Fe$_3$C@N-CNTs/IF exhibited excellent NIRR catalytic performance, with the NO$_3^-$ conversion rate, NH$_3$ production rate and FEs at $-$1.1 V (vs. SCE) reaching 0.786 mg h^{-1} cm^{-2}, 0.922 mg h^{-1} cm^{-2}, and 97.9%, respectively. The electrochemical active surface areas (ECSA) have been evaluated by the electrochemical double layer capacitances (Fig. S17). The ECSA of Fe$_3$C@N-CNTs/IF (21.68 mF cm^{-2}) was much higher than that of Fe$_3$C@CNTs/IF (3.28 mF cm^{-2}) and N-CNTs/IF (1.81 mF cm^{-2}), which means that Fe$_3$C@N-CNTs/IF has much more catalytically active sites for promoting the nitrate conversion rate. These results indicated the significant synergistic effect between Fe$_3$C and N-CNTs. Furthermore, it was revealed by comparing the NIRR performance of Fe$_3$C@N-CNTs/IF and Fe$_3$C@CNTs/IF that the N-doping in CNTs also had a significant impact on the improvement of the NIRR performance.

Density functional theory (DFT) calculations were performed to further explore the source of the catalytic activity of Fe$_3$C@N-CNTs/IF. Based on the characterization results, three simplified models represented of N-CNTs, Fe$_3$C@CNTs, Fe$_3$C@N-CNTs were constructed (Fig. S18). Calculated charge density differences were firstly employed to understand the charge distribution in different models (Fig. 4d-f and
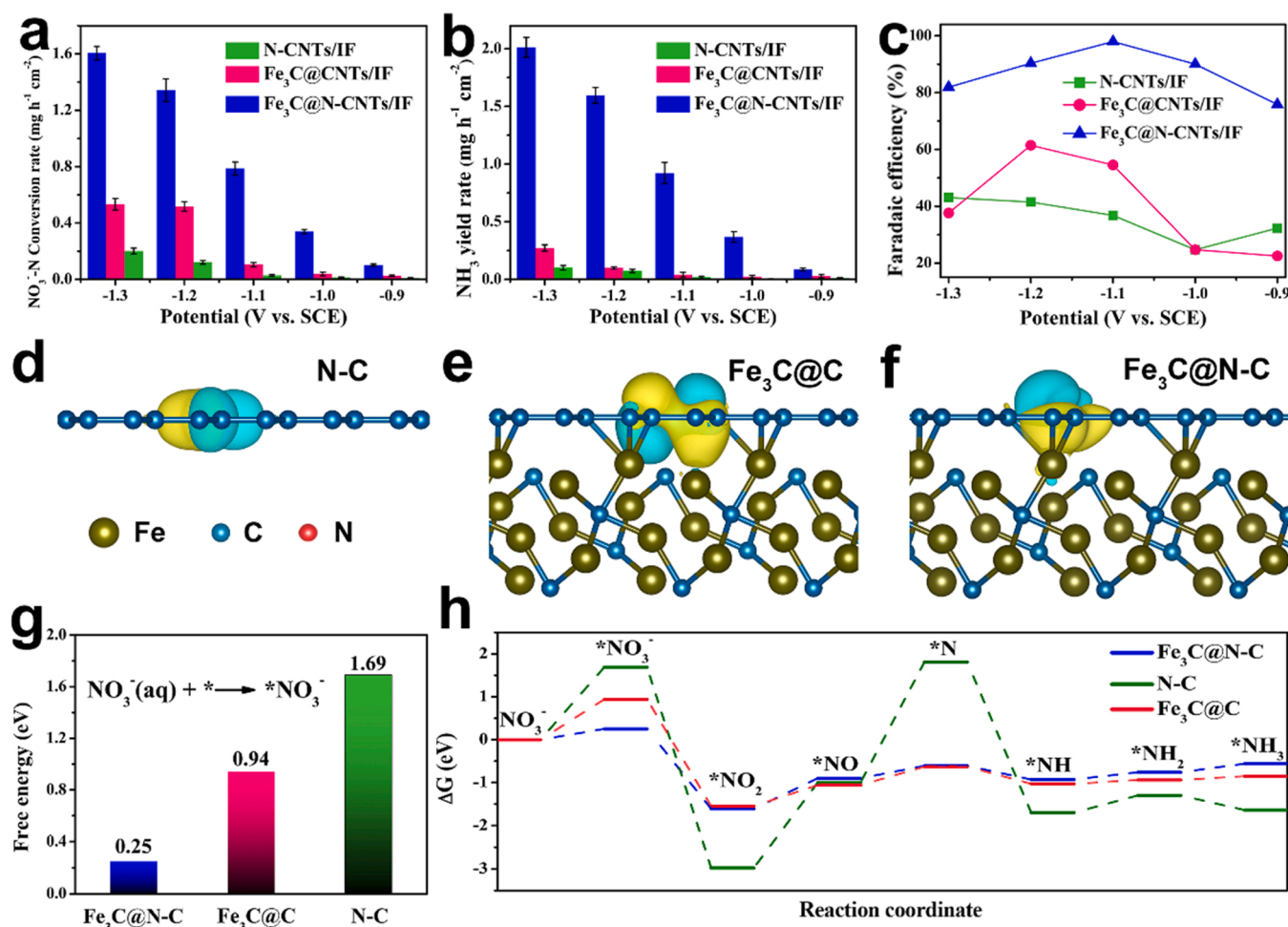
Fig. 4. Comparison of NIRR performance of (a) NO$_3^-$ conversion rate, (b) NH$_3$ yield rates, (c) NH$_3$ FEs of N-CNTs/IF, Fe$_3$C@CNTs/IF and Fe$_3$C@N-CNTs/IF, respectively. Calculated charge density differences of (d) N-C, (e) Fe$_3$C@C and (f) Fe$_3$C@N-C. The isosurface value of the colour region is 0.01 e Å^{-3}. The cyan and yellow regions refer to increased and decreased charge distributions, respectively. (g) Adsorption energies of NO$_3^-$ and (h) Reaction free energies for different intermediates on different models.

S19). Obviously, both the electron density depletion (yellow) and the electron density accumulation (cyan) were shown on the surfaces of N-C and Fe₃C@C. Compared with N-C and Fe₃C@C, there were almost only charge accumulated on the surface of Fe₃C@N-C. Thus, it could be deduced that the strong synergistic interaction between the Fe₃C and N-C in the composite and the doping of nitrogen in carbon shell led to the massive charge aggregation of the surface of Fe₃C@N-CNT, which could effectively reduce the reaction barrier and inhibit the hydrogen evolution reaction as a competitive reaction, resulting in excellent NIRR of Fe₃C@N-CNTs/IF [32,54].

As for the process of NIRR, the first step was the adsorption of NO_3^-, which made a valuable contribution towards the whole catalytic reaction. Therefore, it is thus necessary to evaluate the adsorption energy of NO_3^- on catalysts. As shown in Fig. 4g, it was found that NO_3^- exhibited appropriate adsorption energy on Fe₃C@N-C (0.25 eV). For comparison, the adsorption energy of NO_3^- on the bare N-C (1.69 eV) and Fe₃C@C (0.94 eV) was too strong. Although the electrochemical conversion of NO_3^- to NH_3 was complicated, involving various reactions and

byproducts, this electrochemical reaction $NO_3^- + 6\,H_2O + 8e^- \rightarrow NH_3 + 9OH^-$ could be simplified to a series of deoxidation reactions ($*NO_3^- \rightarrow *NO_2 \rightarrow *NO \rightarrow *N$) and hydrogenation reactions ($*N \rightarrow *NH \rightarrow *NH_2 \rightarrow *NH_3$) [33,56]. The according models and the free energy change of each elementary step on Fe₃C@N-C, N-C and Fe₃C@C were summarized in Fig. S20 and Table S2. As seen in Fig. 4h, for pure N-C and Fe₃C@C, the N * and NO_3^- adsorption were the potential-dependent steps (PDS), respectively. The corresponding U_L values ($U_L = -\Delta G_{max}/e$, where ΔG_{max} was the maximum of free energy change among all elementary steps) reached 1.81 and 0.94 V, respectively. In contrast, the U_L value of Fe₃C@N-C was merely 0.25 V, demonstrating the intense interactions between Fe₃C and N-C, and it was consistent with the calculation result of the charge density difference of Fe₃C@N-C in Fig. 4d-f.

As suggested in previous studies, the type of nitrogen doping in carbon shell could have a significant effect on catalytic performance as well. It was easily achievable to change the temperature (from 700 to 1000 °C) for synthesis of four samples (Fe₃C@N-CNTs/IF-x, x = 700, 800, 900, 1000) with similar microstructure (Fig. S21, S22), but
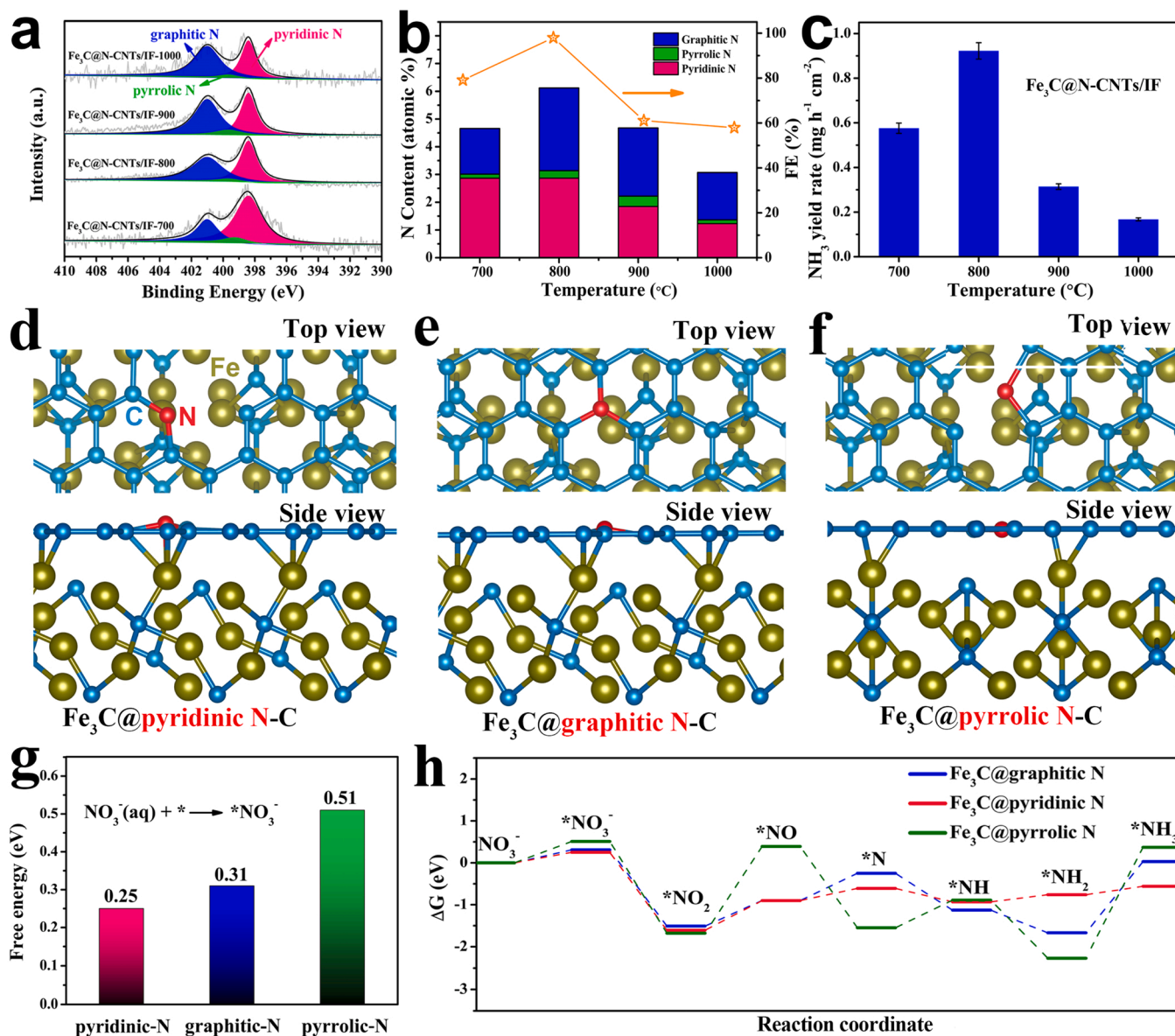
Fig. 5. (a) XPS spectra of N 1 s, (b) configurations of N dopants and FEs, and (c) NH₃ yield rates of Fe₃C@N-CNTs/IF−x (x = 700 −1000). The top and side views of the simplified geometric configurations of Fe₃C coated by (d) pyridinic nitrogen doped carbon, (e) graphite nitrogen doped carbon, and (f) pyrrolic nitrogen doped carbon. (g) adsorption energies of NO_3^- and (h) Reaction free energies for different intermediates on different models.

difference in N species (Fig. 5a, b and S23). As shown in Fig. 5c and S24, the content of nitrogen doping in Fe₃C@N-CNTs/IF-800 was substantially higher compared to other samples, while the NH_3 yield rate (0.922 mg h^{-1} cm^{-2}) and FEs (97.9%) of Fe₃C@N-CNTs/IF-800 was far higher than those of Fe₃C@N-CNTs/IF-700 (0.575 mg h^{-1} cm^{-2} and 79.12%), Fe₃C@N-CNTs/IF-900 (0.314.06 mg h^{-1} cm^{-2} and 61.06%) and Fe₃C@N-CNTs/IF-1000 (0.167 mg h^{-1} cm^{-2} and 57.90%). Apparently, the NIRR performance of Fe₃C@N-CNTs/IF-x was positively correlated with the total amount of nitrogen doped in carbon shell, which is consistent with the above conclusion that nitrogen doping was among the active sources of the Fe₃C@N-CNTs/IF. Moreover, the total amount of nitrogen doping for Fe₃C@N-CNTs/IF-700 (4.66 at%) was similar to that of Fe₃C@N-CNTs/IF-900 (4.68 at%), but the NIRR performance of Fe₃C@N-CNTs/IF-700 was clearly superior to Fe₃C@N-CNTs/IF-900. Therefore, it could be concluded that the pyridine nitrogen in Fe₃C@N-CNTs/IF was more active than graphite nitrogen.

According to the electrocatalytic performances and DFT calculations results as mentioned above, the nitrogen doping on CNT was essential for boosting the catalytic activity. In order to further explore the source of excellent catalytic performance of NIRR, systematic DFT calculations for the different kinds of nitrogen doping were performed. Based on the aforementioned structural characterization, three models (Fe₃C@pyridine N-C, Fe₃C@graphitic N-C and pyrrolic nitrogen (Fe₃C@pyrrolic N-C) were constructed for calculations (Fig. 5d-f). As shown in Fig. 5g, it was found that both Fe₃C@pyridine N-C and Fe₃C@graphitic N-C possessed the appropriate NO_3^- adsorption energies of 0.25 and 0.31 eV, respectively, which were smaller than that of Fe₃C@pyrrolic N-C (0.51 eV). As can be seen from Fig. 5h, the free energy change diagrams of NIRR on Fe₃C@pyridine N-C, Fe₃C@graphitic N-C and Fe₃C@pyrrolic N-C were further analyzed to validate PDS during the conversion from NO_3^- to NH_3. The free energy change of elementary steps were detailed in Table S3, which indicated that the U_L of Fe₃C@-pyridine N-C, Fe₃C@graphitic N-C and Fe₃C@pyrrolic N-C were 0.25, 0.31 and 0.51 V, respectively, suggesting that pyridine N is most conducive for NIRR to produce NH_3.

3.5. Flow cell for NIRR and SOR by porous Fe₃C@N-CNTs/IF electrode

Considering that OER on anode was quite slowly due to the four-electron process, and expended the massive additional electric energy owing to the high theoretical potential (1.23 V vs. RHE), the SOR with fast reaction kinetic was employed as replacement for the OER. In addition, the S derived from SOR on anode had a higher added value than that of O_2. Therefore, compared with (−) NIRR‖OER (+), the designed (−) NIRR‖SOR (+) not only reduced energy consumption but also produced high value-added products of NH_3 and S. The
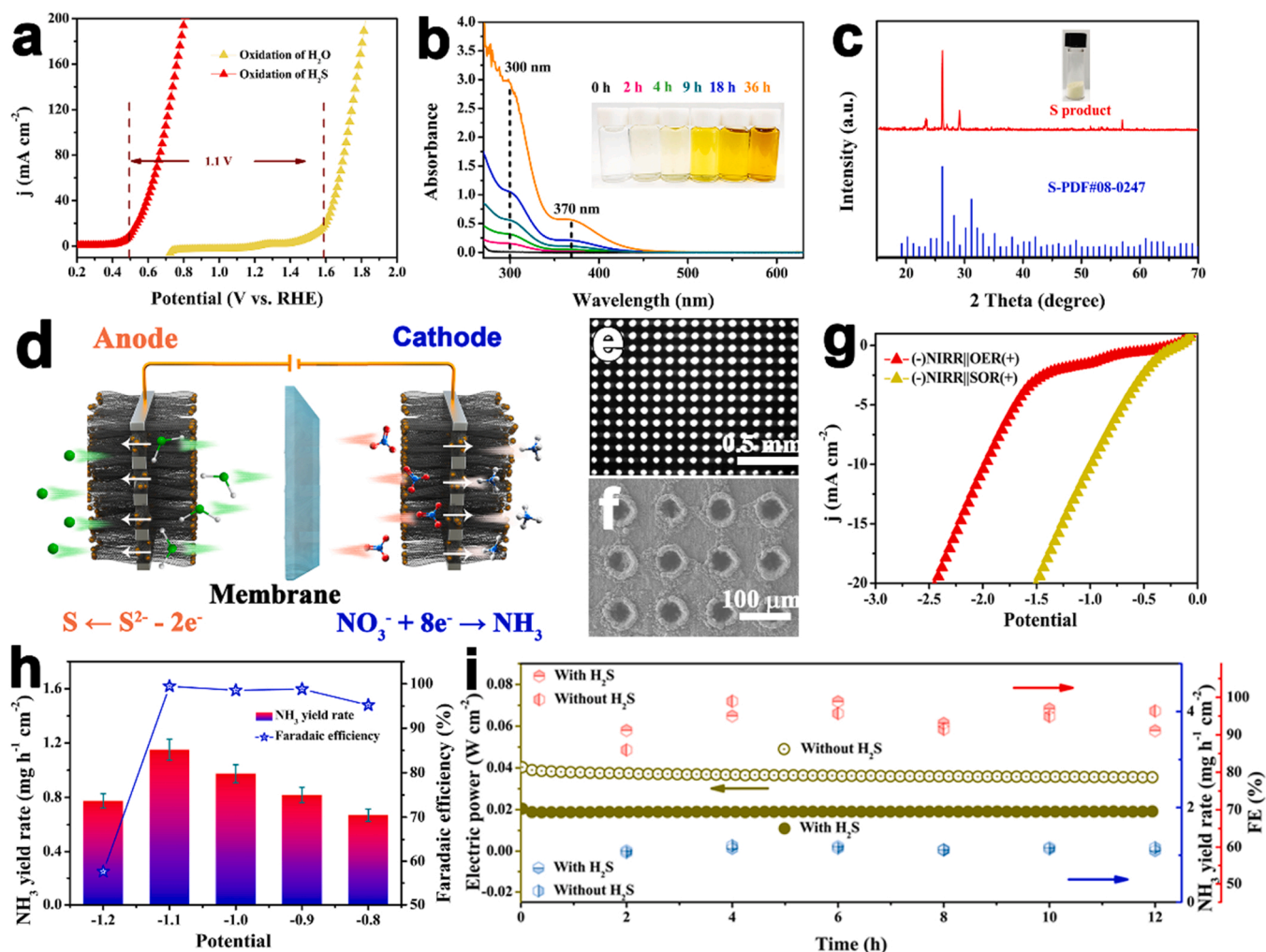
Fig. 6. (a) Comparison of SOR and OER polarization curves for Fe₃C@N-CNTs/IF. (b) UV-Vis spectra of electrolyte and the according photos with the reaction time in a galvanostatic test at 100 mA cm^{-2}. (c) XRD pattern and according photo of product S powder. (d) Concept of the coupled systems of electrolytic NIRR on cathode and SOR on anode in home-made flow-by reactor. (e) Digital image and (f) FESEM image of porous Fe₃C@N-CNTs/IF electrode. (g) Polarization curves of (−) NIRR‖ OER (+) and (−) NIRR‖SOR (+). (h) NH_3 yield rates and FEs at different voltages in flow-by reactor of (−) NIRR ‖ SOR (+). (i) Comparison of electric power, NH_3 yield rates and FEs of (−) NIRR‖OER (+) and (−) NIRR‖SOR (+).

electrocatalytic SOR performance of Fe$_3$C@N-CNTs/IF was investigated with/without S^{2-} in a H-type electrolytic cell (Fig. S25). As plotted in Fig. 6a, the polarization curves of SOR indicated that when the current density reached 10 mA cm^{-2}, the overpotential of SOR was only 0.46 V, which is much lower compare to OER (1.56 V). The potentiostatic test was conducted at a current density of 100 mA cm^{-2}, and the corresponding product in the electrolyte was characterized to measure the production rate of the generated S (Fig. 6b, c). The electrolyte turned yellow and gradually deepened to brown black as time increased, as described in the inset image in Fig. 6b. According to the previous reports, the UV-Vis peaks at 300, 370 and 420 nm could be pointed to the short-chain polysulfides (S$_2^{2-}$-S$_4^{2-}$) in the electrolyte [37,57]. As shown in Fig. 6b, the signal of polysulfide was enhanced with the reaction time. Light yellow powder was collected through simple acid treatment of the electrolyte, and was further confirmed as S by XRD (Fig. 6c). According to calculation, a total of 1215.35 mg S powder with a high yield rate of 33.76 mg h^{-1} cm^{-2} was produced, as shown in Fig. S26. In addition, the high performance of Fe$_3$C@N-CNTs/IF toward SOR outperformed many recently reported nonprecious electrocatalysts and summarized in Table S4.

Given the encouraging results as mentioned above, the flow cell consisting of a coupled of electrodes were designed for eliminating the influence of mass transfer of NO$_3^-$ in the NIRR process and S^{2-} in the SOR process (Fig. 6d and S27), which could overcome the inherent mass transport limitation of a batch type electrochemical cell (H-cell). The designed flow cell was divided into cathode chamber and anode chamber by Nafion-211 membrane. Furthermore, the cathode chamber and anode chamber were divided into two parts by the Fe$_3$C@N-CNTs/IF electrodes with channel made by laser, respectively. As shown in Fig. 6e, f and S28, the channels with a diameter of 50 μm were uniformly distributed across the Fe$_3$C@N-CNTs/IF electrode. The inner wall of the channel was fully covered with Fe$_3$C@N-CNTs, which allowed NIRR and SOR occur in the channel when the electrolyte flowed through the channel. Moreover, the effect of the hole diameter on catalytic performance was also explored, as shown and discussed in Fig. S29 and Text 5 in Supporting information.

As shown in Fig. 6g, the (−) NIRR||SOR (+) flow cell could be driven by the low voltage of 0.99 V to achieve the current density of 10 mA cm^{-2}, which is much lower than that of (−) NIRR||OER (+) (2.2 V). Compared with the static reactor (the NH$_3$ productive rate of 0.922 mg h^{-1} cm^{-2}), the yield in the conceptual flow cell increased to 1.15 mg h^{-1} cm^{-2} and a high FE (98.52%) was maintained, as shown in Fig. 6h and S30, S31. In addition, S powder was produced in the anode chamber with a high yield of 4.87 mg h^{-1} cm^{-2}. In order to explore the reduction of electric energy consumption caused by the coupling of SOR and NIRR, the constant current tests of (−) NIRR||SOR (+) and (−) NIRR||OER (+) were performed, respectively (Fig. 6i and S32). In comparison with the (−) NIRR||OER (+) cell (35.59 mW cm^{-2}), the energy consumption of the (−) NIRR||SOR (+) cell was 16.18 mW cm^{-2}, which means a reduction by nearly half. Undoubtedly, a reasonable designing of the flow-through reactor of (−) NIRR||SOR (+) could contribute to the simultaneous upgradation and utilization of two pollutants (NO$_3^-$ and H$_2$S) to value-added produces (NH$_3$ and S) at low energy costs.

4. Conclusion

In conclusion, we reported a remarkable Fe$_3$C@N-CNTs/IF as a bifunctional electrode for the highly efficient electrocatalytic upcycling of both NO$_3^-$ to NH$_3$ and H$_2$S to S, respectively. The optimized Fe$_3$C@N-CNTs/IF exhibited a superior NIRR performance with the average NH$_3$ production rate of ~0.922 mg h^{-1} cm^{-2} and FE of 97.9% at − 1.1 V vs. SCE. Additionally, it also demonstrated an excellent ability toward SOR, and the yield rate of S from H$_2$S oxidation was reached up to 33.76 mg h^{-1} cm^{-2} at the current density of 100 mA cm^{-2}. DFT calculations demonstrated that the catalytic activity of carbon shell was

promoted by the adjustment of inner Fe$_3$C core and nitrogen dopants, resulting in a robust electrocatalytic activity. Eventually, a proof-of-concept electrochemical flow reactor was developed for employing Fe$_3$C@N-CNTs/IF with channels toward electrochemical NO$_3^-$ reduction and H$_2$S oxidation, showing the increased NH$_3$ yield rate of 1.15 mg h^{-1} cm^{-2}. Undoubtedly, the reasonable design of the flow-by reactor of (−) NIRR||SOR (+) is conducive to the simultaneously elimination and utilization of two sorts of pollutants (NO$_3^-$ and H$_2$S) to value-added produces (NH$_3$ and S) at low energy consumption.

CRediT authorship contribution statement

W. Yu, J. Yu and W. Zhou conceived the idea and designed the experiments. **W. Yu** performed the fabrication, measurement, and analysis of the catalysts. **W. Yu and Y. Wang** conducted the electrochemical measurements and data analysis. **X. Li.** conducted the TEM measurements. **Y. Wang, H. Yuan and X. Zhang** conducted the DFT theoretical calculations and data analysis. **W. Yu, J. Yu, H. Liu and W. Zhou** prepared the manuscript. All authors discussed and commented on the manuscript. **J. Yu and W. Zhou** supervised the project.

Declaration of Competing Interest

The authors declare that they have no known competing financial interests or personal relationships that could have appeared to influence the work reported in this paper.

Acknowledgements

Appendix A. Supporting information

Supplementary data associated with this article can be found in the online version at doi:10.1016/j.apcatb.2022.121291.

References

[1] C. Tang, S. Qiao, How to explore ambient electrocatalytic nitrogen reduction reliably and insightfully, Chem. Soc. Rev. 48 (2019) 3166–3180, https://doi.org/10.1039/C9CS00280D.

[2] S. Foster, S. Bakovic, R. Duda, S. Maheshwari, R. Milton, S. Minteer, M. Janik, J. Renner, L. Greenlee, Catalysts for nitrogen reduction to ammonia, Nat. Catal. 1 (2018) 490–500, https://doi.org/10.1039/C9CS00280D.

[3] Y. Ashida, K. Arashiba, K. Nakajima, Y. Nishibayashi, Molybdenum-catalysed ammonia production with samarium diiodide and alcohols or water, Nature 568 (2019) 536–540, https://doi.org/10.1038/s41586-019-1134-2.

[4] Y. Zhao, B. Setzler, J. Wang, J. Nash, T. Wang, B. Xu, Y. Yan, An efficient direct ammonia fuel cell for affordable carbon-neutral transportation, Joule 3 (2019) 2472–2484, https://doi.org/10.1016/j.joule.2019.07.005.

[5] M. Assumpcao, R. Piasentin, P. Hammer, R. De Souza, G. Buzzo, M. Santos, E. Spinace, A. Neto, J. Silva, Oxidation of ammonia using PtRh/C electrocatalysts: fuel cell and electrochemical evaluation, Appl. Catal. B: Environ. 174–175 (2015) 136–144, https://doi.org/10.1016/j.apcatb.2015.02.021.

[6] R. Hawtof, S. Ghosh, E. Guarr, C. Xu, R. Mohan Sankaran, N. Renner Julie, Catalyst-free, highly selective synthesis of ammonia from nitrogen and water by a plasma electrolytic system, Sci. Adv. 5 5 (2019) eaat5778, https://doi.org/10.1126/sciadv.aat5778.

[7] Y. Wan, J. Xu, R. Lv, Heterogeneous electrocatalysts design for nitrogen reduction reaction under ambient conditions, Mater. Today 27 (2019) 69–90, https://doi.org/10.1016/j.mattod.2019.03.002.

[8] G. Soloveichik, Electrochemical synthesis of ammonia as a potential alternative to the Haber–Bosch process, Nat. Catal. 2 (2019) 377–380, https://doi.org/10.1038/s41929-019-0280-0.

[9] B. Suryanto, H. Du, D. Wang, J. Chen, A. Simonov, D. MacFarlane, Challenges and prospects in the catalysis of electroreduction of nitrogen to ammonia, Nat. Catal. 2 (2019) 290–296, https://doi.org/10.1038/s41929-019-0252-4.

[10] M. Kitano, Y. Inoue, Y. Yamazaki, F. Hayashi, S. Kanbara, S. Matsuishi, T. Yokoyama, S. Kim, M. Hara, H. Hosono, Ammonia synthesis using a stable

electride as an electron donor and reversible hydrogen store, Nat. Chem. 4 (2012) 934–940, https://doi.org/10.1038/nchem.1476.

[11] A. Wu, J. Yang, B. Xu, X. Wu, Y. Wang, X. Lv, Y. Ma, A. Xu, J. Zheng, Q. Tan, Y. Peng, Z. Qi, H. Qi, J. Li, Y. Wang, J. Harding, X. Tu, A. Wang, J. Yan, X. Li, Direct ammonia synthesis from the air via gliding arc plasma integrated with single atom electrocatalysis, Appl. Catal. B: Environ. 299 (2021), 120667, https://doi.org/10.1016/j.apcatb.2021.120667.

[12] S. Licht, B. Cui, B. Wang, F. Li, J. Lau, S. Liu, Ammonia synthesis by N_2 and steam electrolysis in molten hydroxide suspensions of nanoscale Fe_2O_3, Science 345 (2014) 637–640, https://doi.org/10.1126/science.1254234.

[13] W. Zhu, T. Zhang, Y. Zhang, Z. Yue, Y. Li, R. Wang, Y. Ji, X. Sun, J. Wang, A practical-oriented NiFe-based water-oxidation catalyst enabled by ambient redox and hydrolysis co-precipitation strategy, Appl. Catal. B: Environ. 244 (2019) 844–852, https://doi.org/10.1016/j.apcatb.2018.12.021.

[14] X. Zhang, Y. Wang, C. Liu, Y. Yu, S. Lu, B. Zhang, Recent advances in non-noble metal electrocatalysts for nitrate reduction, Chem. Eng. J. 403 (2021), 126269, https://doi.org/10.1016/j.cej.2020.126269.

[15] G. Chen, X. Cao, S. Wu, X. Zeng, L. Ding, M. Zhu, H. Wang, Ammonia electrosynthesis with high selectivity under ambient conditions via a Li^+ incorporation strategy, J. Am. Chem. Soc. 139 (2017) 9771–9774, https://doi.org/10.1021/jacs.7b04393.

[16] Y. Song, D. Johnson, R. Peng, K. Hensley Dale, V. Bonnesen Peter, L. Liang, J. Huang, F. Yang, F. Zhang, R. Qiao, P. Baddorf Arthur, J. Tschaplinski Timothy, L. Engle Nancy, C. Hatzell Marta, Z. Wu, A. Cullen David, M. Meyer Harry, G. Sumpter Bobby, J. Rondinone Adam, A physical catalyst for the electrolysis of nitrogen to ammonia, Sci. Adv. 4 (2018), e1700336, https://doi.org/10.1126/sciadv.1700336.

[17] P. Chen, N. Zhang, S. Wang, T. Zhou, Y. Tong, C. Ao, W. Yan, L. Zhang, W. Chu, C. Wu, Y. Xie, Interfacial engineering of cobalt sulfide/graphene hybrids for highly efficient ammonia electrosynthesis, Proc. Natl. Acad. Sci. 116 (2019) 6635–6640, https://doi.org/10.1073/pnas.1817881116.

[18] J. Wang, L. Yu, L. Hu, G. Chen, H. Xin, X. Feng, Ambient ammonia synthesis via palladium-catalyzed electrohydrogenation of dinitrogen at low overpotential, Nat. Commun. 9 (2018) 1795, https://doi.org/10.1038/s41467-018-04213-9.

[19] X. Cui, C. Tang, Q. Zhang, A review of electrocatalytic reduction of dinitrogen to ammonia under ambient conditions, Adv. Energy Mater. 8 (2018) 1800369, https://doi.org/10.1002/aenm.201800369.

[20] K. Chu, Y. Liu, Y. Li, Y. Guo, Y. Tian, H. Zhang, Multi-functional Mo-doping in MnO_2 nanoflowers toward efficient and robust electrocatalytic nitrogen fixation, Appl. Catal. B: Environ. 264 (2020), 118525, https://doi.org/10.1016/j.apcatb.2019.118525.

[21] Z. Geng, Y. Liu, X. Kong, P. Li, K. Li, Z. Liu, J. Du, M. Shu, R. Si, J. Zeng, Achieving a record-high yield rate of 120.9 for N_2 electrochemical reduction over Ru single-atom catalysts, Adv. Mater. 30 (2018), 1803498, https://doi.org/10.1002/adma.201803498.

[22] C. Lv, C. Yan, G. Chen, Y. Ding, J. Sun, Y. Zhou, G. Yu, An amorphous noble-metal-free electrocatalyst that enables nitrogen fixation under ambient conditions, Angew. Chem. Int. Ed. 57 (2018) 6073–6076, https://doi.org/10.1002/anie.201801538.

[23] S. Andersen, V. ColiC, S. Yang, J. Schwalbe, A. Nielander, J. McEnaney, K. Enemark-Rasmussen, J. Baker, A. Singh, B. Rohr, M. Statt, S. Blair, S. Mezzavilla, J. Kibsgaard, P. Vesborg, M. Cargnello, S. Bent, T. Jaramillo, I. Stephens, J. Norskov, I. Chorkendorff, A rigorous electrochemical ammonia synthesis protocol with quantitative isotope measurements, Nature 570 (2019) 504–508, https://doi.org/10.1038/s41586-019-1260-x.

[24] B. Chang, L. Li, D. Shi, H. Jiang, Z. Ai, S. Wang, Y. Shao, J. Shen, Y. Wu, Y. Li, X. Hao, Metal-free boron carbonitride with tunable boron Lewis acid sites for enhanced nitrogen electroreduction to ammonia, Appl. Catal. B: Environ. 283 (2021), 119622, https://doi.org/10.1016/j.apcatb.2020.119622.

[25] L. Su, D. Han, G. Zhu, H. Xu, W. Luo, L. Wang, W. Jiang, A. Dong, J. Yang, Tailoring the assembly of iron nanoparticles in carbon microspheres toward high-performance electrocatalytic denitrification, Nano Lett. 19 (2019) 5423–5430, https://doi.org/10.1021/acs.nanolett.9b01925.

[26] C. Yu, X. Huang, H. Chen, H. Godfray, J. Wright, J. Hall, P. Gong, S. Ni, S. Qiao, G. Huang, Y. Xiao, J. Zheng, Z. Feng, X. Ju, P. Ciais, N. Stenseth, D. Hessen, Z. Sun, L. Yu, W. Cai, H. Fu, X. Huang, C. Zhang, H. Liu, J. Taylor, Managing nitrogen to restore water quality in China, Nature 567 (2019) 516–520, https://doi.org/10.1038/s41586-019-1001-1.

[27] G. Cerron-Calle, A. Fajardo, C. Sanchez-Sanchez, S. Garcia-Segura, Highly reactive Cu-Pt bimetallic 3D-electrocatalyst for selective nitrate reduction to ammonia, Appl. Catal. B: Environ. 302 (2022), 120844, https://doi.org/10.1016/j.apcatb.2021.120844.

[28] Y. Li, J. Ma, T. Waite, M. Hoffmann, Z. Wang, Development of a mechanically flexible 2D-MXene membrane cathode for selective electrochemical reduction of nitrate to N_2: mechanisms and implications, Environ. Sci. Techn. 55 (2021) 10695–10703, https://doi.org/10.1021/acs.est.1c00264.

[29] J. Sun, W. Gao, H. Fei, G. Zhao, Efficient and selective electrochemical reduction of nitrate to N_2 by relay catalytic effects of Fe-Ni bimetallic sites on MOF-derived structure, Appl. Catal. B: Environ. 301 (2022), 120829, https://doi.org/10.1016/j.apcatb.2021.120829.

[30] M. Mladenovic, M. Paprika, A. Marinkovic, Denitrification techniques for biomass combustion, Renew. Sust. Energ. Rev. 82 (2018) 3350–3364, https://doi.org/10.1016/j.rser.2017.10.054.

[31] S. Lee, S. Kim, C. Park, W. Kim, S. Ryu, W. Choi, Solar denitrification coupled with in situ water splitting, Energy Environ. Sci. 14 (2021) 4437–4450, https://doi.org/10.1039/D1EE01342D.

[32] Y. Wang, W. Zhou, R. Jia, Y. Yu, B. Zhang, Unveiling the activity origin of a copper-based electrocatalyst for selective nitrate reduction to ammonia, Angew. Chem. Int. Ed. 59 (2020) 5350–5354, https://doi.org/10.1002/anie.201915992.

[33] Y. Wang, A. Xu, Z. Wang, L. Huang, J. Li, F. Li, J. Wicks, M. Luo, D. Nam, C. Tan, Y. Ding, J. Wu, Y. Lum, C. Dinh, D. Sinton, G. Zheng, E. Sargent, Enhanced nitrate-to-ammonia activity on copper–nickel alloys via tuning of intermediate adsorption, J. Am. Chem. Soc. 142 (2020) 5702–5708, https://doi.org/10.1021/jacs.9b13347.

[34] Y. Zeng, C. Priest, G. Wang, G. Wu, Restoring the nitrogen cycle by electrochemical reduction of nitrate: progress and prospects, Small Methods 4 (2020), 2000672, https://doi.org/10.1002/smtd.202000672.

[35] S. Garcia-Segura, M. Lanzarini-Lopes, K. Hristovski, P. Westerhoff, Electrocatalytic reduction of nitrate: fundamentals to full-scale water treatment applications, Appl. Catal. B: Environ. 236 (2018) 546–568, https://doi.org/10.1016/j.apcatb.2018.05.041.

[36] M. Duca, M. Koper, Powering denitrification: the perspectives of electrocatalytic nitrate reduction, Energy Environ. Sci. 5 (2012) 9726–9742, https://doi.org/10.1039/C2EE23062C.

[37] M. Zhang, M. Guan, Y. Tu, S. Chen, Y. Wang, S. Wang, L. Yu, C. Ma, D. Deng, X. Bao, Highly efficient H_2 production from H_2S via a robust graphene-encapsulated metal catalyst, Energy Environ. Sci. 13 (2020) 119–126, https://doi.org/10.1039/C9EE03231B.

[38] X. Chen, T. Zhang, M. Kan, D. Song, J. Jia, Y. Zhao, X. Qian, Binderless and oxygen vacancies rich FeNi/graphitized mesoporous carbon/Ni foam for electrocatalytic reduction of nitrate, Environ. Sci. Techno. 54 (2020) 13344–13353, https://doi.org/10.1021/acs.est.0c05631.

[39] Q. Zhang, X. Li, B. Tao, X. Wang, Y. Deng, X. Gu, L. Li, W. Xiao, N. Li, H. Luo, CoNi based alloy/oxides@N-doped carbon core-shell dendrites as complementary water splitting electrocatalysts with significantly enhanced catalytic efficiency, Appl. Catal. B: Environ. 254 (2019) 634–646, https://doi.org/10.1016/j.apcatb.2019.05.035.

[40] M. Li, H. Li, X. Jiang, M. Jiang, X. Zhan, G. Fu, J. Lee, Y. Tang, Gd-induced electronic structure engineering of a NiFe-layered double hydroxide for efficient oxygen evolution, J. Mater. Chem. A 9 (2021) 2999–3006, https://doi.org/10.1039/D0TA10740A.

[41] J. Zhang, Y. Yan, B. Mei, R. Qi, T. He, Z. Wang, W. Fang, S. Zaman, Y. Su, S. Ding, B. Xia, Local spin-state tuning of cobalt–iron selenide nanoframes for the boosted oxygen evolution, Energy Environ. Sci. 14 (2021) 365–373, https://doi.org/10.1039/D0EE03500A.

[42] H. Yang, L. Gong, H. Wang, C. Dong, J. Wang, K. Qi, H. Liu, X. Guo, B. Xia, Preparation of nickel-iron hydroxides by microorganism corrosion for efficient oxygen evolution, Nat. Commun. 11 (2020) 5075, https://doi.org/10.1038/s41467-020-18891-x.

[43] J. Yu, G. Li, H. Liu, L. Zeng, L. Zhao, J. Jia, M. Zhang, W. Zhou, H. Liu, Y. Hu, Electrochemical flocculation integrated hydrogen evolution reaction of Fe@N-doped carbon nanotubes on iron foam for ultralow voltage electrolysis in neutral media, Adv. Sci. 6 (2019), 1901458, https://doi.org/10.1002/advs.201901458.

[44] R. Li, K. Xiang, Z. Peng, Y. Zou, S. Wang, Recent advances on electrolysis for simultaneous generation of valuable chemicals at both anode and cathode, Adv. Energy Mater. 11 (2021), 2102292, https://doi.org/10.1002/aenm.202102292.

[45] W. Ma, C. Xie, X. Wang, H. Wang, X. Jiang, H. Zhang, X. Guo, X. Zong, X. Li, C. Li, High-performance solar redox flow battery toward efficient overall splitting of hydrogen sulfide, ACS Energy Lett. 5 (2020) 597–603, https://doi.org/10.1021/acsenergylett.9b02206.

[46] D. Meyer, R. Prien, L. Rautmann, M. Pallentin, J. Waniek, D. Schulz-Bull, In situ determination of nitrate and hydrogen sulfide in the baltic sea using an ultraviolet spectrophotometer, Front. Mar. Sci. 5 (2018) 431, https://doi.org/10.3389/fmars.2018.00431.

[47] W. Zhou, J. Jia, J. Lu, L. Yang, D. Hou, G. Li, S. Chen, Recent developments of carbon-based electrocatalysts for hydrogen evolution reaction, Nano Energy 28 (2016) 29–43, https://doi.org/10.1016/j.nanoen.2016.08.027.

[48] H. Fan, L. Qiu, A. Fedorov, M. Willinger, F. Ding, X. Huang, Dynamic state and active structure of Ni–Co catalyst in carbon nanofiber growth revealed by in situ transmission electron microscopy, ACS Nano 15 (2021) 17895–17906, https://doi.org/10.1021/acsnano.1c06189.

[49] Y. Zhao, J. Zhang, X. Guo, H. Fan, W. Wu, H. Liu, G. Wang, Fe_3C@nitrogen doped CNT arrays aligned on nitrogen functionalized carbon nanofibers as highly efficient catalysts for the oxygen evolution reaction, J. Mater. Chem. A 5 (2017) 19672–19679.

[50] D. Fletcher, R. Hunter, W. Xia, G. Smales, B. Pauw, E. Blackburn, A. Kulak, H. Xin, Z. Schnepp, Scalable synthesis of dispersible iron carbide (Fe_3C) nanoparticles by 'nanocasting', J. Mater. Chem. A 7 (2019) 19506–19512, https://doi.org/10.1039/C9TA06876G.

[51] P. Tan, Active phase, catalytic activity, and induction period of Fe/zeolite material in nonoxidative aromatization of methane, J. Catal. 338 (2016) 21–29, https://doi.org/10.1016/j.jcat.2016.01.027.

[52] Y. Wang, C. Wang, M. Li, Y. Yu, B. Zhang, Nitrate electroreduction: mechanism insight, in situ characterization, performance evaluation, and challenges, Chem. Soc. Rev. 50 (2021) 6720–6733, https://doi.org/10.1039/D1CS00116G.

[53] R. Jia, Y. Wang, C. Wang, Y. Ling, Y. Yu, B. Zhang, Boosting selective nitrate electroreduction to ammonium by constructing oxygen vacancies in TiO_2, ACS Catal. 10 (2020) 3533–3540, https://doi.org/10.1021/acscatal.9b05260.

[54] Y. Guo, R. Zhang, S. Zhang, Y. Zhao, Q. Yang, Z. Huang, B. Dong, C. Zhi, Pd doping-weakened intermediate adsorption to promote electrocatalytic nitrate reduction on TiO_2 nanoarrays for ammonia production and energy supply with zinc–nitrate batteries, Energy Environ. Sci. 14 (2021) 3938–3944, https://doi.org/10.1039/D1EE00806D.

[55] X. Zhao, F. Li, R. Wang, J. Seo, H. Choi, S. Jung, J. Mahmood, I. Jeon, J. Baek, Controlled fabrication of hierarchically structured nitrogen-doped carbon nanotubes as a highly active bifunctional oxygen electrocatalyst, Adv. Funct. Mater. 27 (2017), 1605717, https://doi.org/10.1002/adfm.201605717.

[56] J. Liu, D. Richards, N. Singh, B. Goldsmith, Activity and selectivity trends in electrocatalytic nitrate reduction on transition metals, ACS Catal. 9 (2019) 7052–7064, https://doi.org/10.1021/acscatal.9b02179.

[57] Y. Pei, J. Cheng, H. Zhong, Z. Pi, Y. Zhao, F. Jin, Sulfide-oxidation-assisted electrochemical water splitting for H_2 production on a bifunctional Cu_2S/nickel foam catalyst, Green. Chem. 23 (2021) 6975–6983, https://doi.org/10.1039/D1GC01857D.